Nitish Anand
Propulsion & Power,
Aerospace Engineering Faculty,
Delft University of Technology,
Kluyverweg 1,
Delft 2629 HS, The Netherlands
e-mail: N.Anand@tudelft.nl

Salvatore Vitale
Propulsion & Power,
Aerospace Engineering Faculty,
Delft University of Technology,
Kluyverweg 1,
Delft 2629 HS, The Netherlands
e-mail: S.Vitale@tudelft.nl

Matteo Pini[1]
Propulsion & Power,
Aerospace Engineering Faculty,
Delft University of Technology,
Kluyverweg 1,
Delft 2629 HS, The Netherlands
e-mail: M.Pini@tudelft.nl

Gustavo J. Otero
Energy Technology,
Mechanical Engineering Faculty,
Delft University of Technology,
Leeghwaterstraat 39,
Delft 2628 CB, The Netherlands
e-mail: G.J.OteroRodriguez@tudelft.nl

Rene Pecnik
Energy Technology,
Mechanical Engineering Faculty,
Delft University of Technology,
Leeghwaterstraat 39,
Delft 2628 CB, The Netherlands
e-mail: R.Pecnik@tudelft.nl

Design Methodology for Supersonic Radial Vanes Operating in Nonideal Flow Conditions

The stator vanes of high-temperature organic Rankine cycle (ORC) radial-inflow turbines (RIT) operate under severe expansion ratios and the associated fluid-dynamic losses account for nearly two-thirds of the total losses generated within the blading passages. The efficiency of the machine can strongly benefit from specialized high-fidelity design methods able to provide shapes attenuating shock wave formation, consequently reducing entropy generation across the shock-wave and mitigating shock-wave boundary layer interaction. Shape optimization is certainly a viable option to deal with supersonic ORC stator design, but it is computationally expensive. In this work, a robust method to approach the problem at reduced computational cost is documented. The method consists of a procedure encompassing the method of characteristics (MoC), extended to nonideal fluid flow, for profiling the diverging part of the nozzle. The subsonic section and semi-bladed suction side are retrieved using a simple conformal geometrical transformation. The method is applied to design a supersonic ORC stator working with Toluene vapor, for which two blade shapes were already available. The comparison of fluid-dynamic performance clearly indicates that the MoC-Based method is able to provide the best results with the lowest computational effort, and is therefore suitable to be used in a systematic manner for drawing general design guidelines. [DOI: 10.1115/1.4040182]

1 Introduction

When small power output, large flow coefficients, and large work coefficients are of concern, the radial-inflow turbine (RIT) is the typical configuration of choice. This kind of turbomachinery is usually constituted by a single stage accommodating the entire expansion ratio. Key advantages over axial turbines are the inherent compactness and the much lower sensitivity to tip clearance losses, which is highly favorable at downsized scales [1].

Thanks to these characteristics, mobile and stationary systems exploiting RITs are vast. For example, in diverse configurations, RITs have found wide application for waste heat recovery in internal combustion engines [2,3] and power generation in microgas turbines [4]. Despite their bulkiness and heavy weight, radial turbines have also started receiving recognition for space systems. The work of Ref. [5] pointed out that RITs can replace axial turbines [6–9] for driving rocket turbopumps, essentially because they perform better than axial turbines at high velocity ratios and they can better deal with varying incidence angles, besides featuring lower stress levels than axial configurations. RITs are furthermore largely utilized in power generation units and air liquefaction plants [10,11]. A more recent, but rapidly growing domain of application for RITs is as expanders in mini and small high-temperature organic Rankine cycle (ORC) power systems [12–14]. The recent study performed by Bahamonde et al. [15] showed that for high-temperature mini-ORC applications, i.e., units of power capacity in the order of 3–50 kW$_e$, the RIT outperforms both the axial and the radial-outflow configuration, despite the possibility of splitting the expansion rate over multiple stages in the latter, with consequent fluid-dynamic benefits due to attenuated compressibility effects.

Irrespective of the power level, the development of efficient radial-inflow turbines for small and mini ORCs is still a challenge and the technology is by far not mature yet. One of the principal reasons is that their fluid-dynamic design is significantly more complicated than that of conventional RITs and experimentally derived design guidelines are absent. Small and mini-ORC radial-inflow turbines rotate at high speed and must deal with very large volumetric flow ratios, as high as 60, most of it taking place in the stator. Moreover, the complex organic molecules employed as working medium in mini-ORCs are characterized by a comparatively lower speed of sound and exhibit prominent nonideal gas effects [16,17]. The net result is that the stator of these machines suffers from severe fluid-dynamic penalties due to the onset of strong shock-wave, interacting with either boundary layers or the

---

[1]Corresponding author.

Copyright © 2019 by ASME

trailing edge wake. All these phenomena generally produce highly nonuniform flows entering the rotor, giving possible rise to flow separation in the rotating blade passages [18]. The optimal profiling of the stator is therefore challenging and a poor design can hinder the attainment of acceptable turbine performance, which is deemed essential to make ORC technology ultimately viable. As shown in Ref. [19], the stator vane is responsible for almost twice the losses generated in the rotor cascade, testifying the importance to focus on stator design. This is the scope of the present work.

Recently, ORC turbines have been designed using geometrical similarities based on preliminary design [20], method of characteristics (MoC) for supersonic axial stator and rotor [7], and by using parametrized shape optimization [21]. To date, only few design methods have been proposed to perform the design of supersonic radial stator vanes. In Ref. [19], a method to design a radial stator geometry based on a simplified MoC extended to nonideal flows is illustrated. In Ref. [22], a straight-axis stator is designed for a RIT by locating nozzles in the geometrical constraints of the turbine. In Ref. [23], the authors used automated computational fluid dynamics (CFD)-based blade shape optimization to accomplish the optimal design of a centripetal stator operating with Toluene vapor.

In this work, a novel method to design radial supersonic vanes operating with nonideal flows is proposed. The method encompasses the MoC extended to nonideal fluid flows and a geometrical transformation procedure. More specifically, the supersonic diverging section of the vane is initially constructed by using the MoC for nonideal flows, adapted from Refs. [22] and [24]. The resulting channel profile is then conformally-mapped into the radial frame of reference to preserve the desired flow outlet angle. Finally, an automated geometrical procedure is developed to accomplish the converging, subsonic part, and the semibladed suction side profile by ensuring that the thickness of the trailing edge equals the minimum value allowed by manufacturing constraints.

The effectiveness of the proposed method is demonstrated by designing a supersonic radial stator for a typical high-temperature small ORC turbine. The fluid-dynamic performance of the stator is compared to that of the two stator vane configurations developed previously for the same turbine. The fluid-dynamic loss coefficients of the three vanes are assessed using a Reynolds-Averaged Navier–Stokes model based on accurate thermodynamic equations of state and first design recommendations are finally formulated based on the obtained results.

2 Design Procedure

The design method consists of two main steps: first, the diverging section of the supersonic stator is designed by means of the MoC, then the shape of the blade is constructed through a geometrical transformation.

2.1 Design of the Bladed Diverging Section. Method of characteristics is a marching type analytical method to solve hyperbolic partial differential equations. It is a classical method to design the diverging section of the supersonic nozzle under the assumption of steady homentropic flow [25,26]. Such a flow is governed by the two-dimensional isentropic Euler equations.

In order to initialize the calculation method, the sonic line must be determined. In this work, the approach proposed in Ref. [27] extended to nonideal fluid flow as in Ref. [24] was adopted. Then, the construction of the diverging section proceeds as follows: the channel is decomposed in two different, consecutive regions. The former, usually termed as kernel region, is defined by imposing a circular radius connecting the throat to the point from which the departing expansion wave leads to the desired outlet Mach number at the centerline axis of the nozzle. The latter, called reflex region, is defined by imposing mass conservation between the kernel and the reflex region. The primary function of the kernel region is to generate expansion waves to accelerate the flow to the

desired Mach number (Ma), while the reflex region is designed to deviate the flow such as to obtain uniform conditions at nozzle exit.

At each point along the expansion, the flow conditions, i.e., velocity component and magnitude, are retrieved by solving the two families of compatibility and characteristic equations:

$$\lambda_{\pm} = \tan(\phi \pm \alpha) \qquad (1)$$

$$(u^2 - c^2)du_{\pm} + (v^2 - c^2)\lambda_{\pm}^{-1}dv_{\pm} = 0 \qquad (2)$$

where λ is the characteristic slope, ϕ is the flow angle, α is the Mach angle, c is the speed of sound and, and u and v are the velocities in x and y directions, respectively. Equations (1) and (2) represent the characteristic (Mach wave) and the compatibility equation. The subscripts $+$ and $-$ represent the two families of characteristic lines, which hold for a point in the supersonic flow regime.

Starting from the sonic line, the position of a subsequent point in either the kernel or the reflex region is determined by using the characteristic equation. More specifically, the characteristic equation defines the direction of a pressure wave at a given point (from each point two waves with slope opposite in sign, i.e., $\pm$, depart). By intersecting the two characteristic waves $\pm$ departing from two adjacent points, the location (x, y) of a new point is retrieved. The compatibility equation of the intersecting waves is then solved simultaneously to calculate the velocity components (u, v) at the new point. At this node, the speed of sound (c) is calculated using an arbitrary equation of state as:

$$c = c(H, s) \qquad (3)$$

where s is the inlet entropy and H is the static enthalpy. The two properties can be computed as follows:

$$s = s(P_{\text{tot}}, T_{\text{tot}}) \qquad (4)$$

$$H = H(V, H_{\text{tot}}) = H_{\text{tot}}(P_{\text{tot}}, T_{\text{tot}}) - V^2/2 \qquad (5)$$

where P_{tot} and T_{tot} are the total upstream conditions and V is the flow velocity. The Mach angle and flow angle are eventually attained as:

$$\alpha = \arcsin(1/M) \qquad (6)$$

$$\phi = \arctan(v/u) \qquad (7)$$

The calculation is marched in space until the prescribed nozzle outlet conditions are met. Figure 1 displays the ensemble of points encompassing the diverging nozzle section obtained by the MoC. In order to account for nonideal fluid effects, which typically occur in the supersonic stator of ORC turbines, the multiparameter Span and Wagner equation of state [28], available in FluidProp [29], is adopted to compute these thermodynamic quantities, specifically Eqs. (3)–(5).

The shape of the diverging nozzle strongly depends on the working fluid and thermodynamic conditions where the expansion process takes place. Typically, a fairly complex fluid like toluene results in a longer and larger nozzle than compared to Air. For example, the nozzle reported in Fig. 2 illustrates nozzle profile for same outlet Mach number, but using air (assumed as perfect gas) and toluene in nonideal flow conditions (with a compressibility factor of 0.7 at the throat).

2.2 Design of the Radial Stator Vane. The shape of the supersonic radial vane is obtained by complementing the diverging section designed by MoC with the converging part, both adapted to fit in the radial frame of reference. The detailed procedure is as follows:
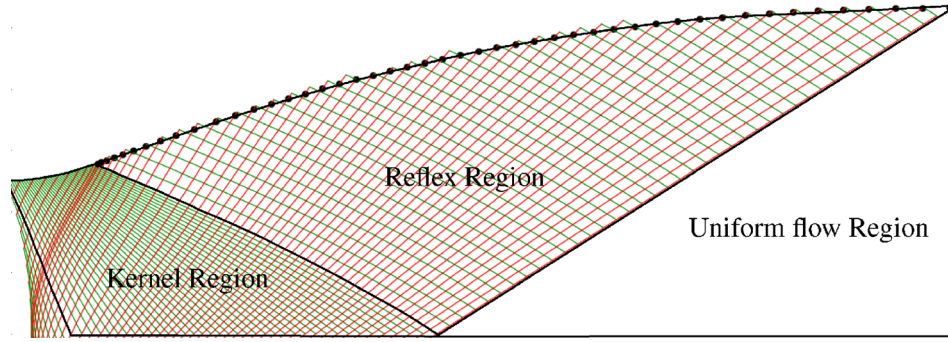
Fig. 1 Method of characteristics implemented to design the diverging section of the super-sonic nozzle. The lines with positive slope represent positive characteristics and those with negative slope are negative characteristics.

(1) *Position the diverging section of the nozzle at R_{out}*. First, the coordinates of the diverging section of the nozzle are scaled by using an initial scaling factor S equal to half of the radial chord. Next, the diverging profile is shifted and rotated in such a way that (i) the trailing edge of the pressure side of the diverging nozzle section (point n_{b2}) is positioned at R_{out} (see gray nozzle in Fig. 3) and (ii) the design flow angle ϕ at the nozzle centerline exit section matches the prescribed radial flow angle of the vane.

(2) *Map the diverging section into the radial frame of reference*. The diverging section obtained in step 1 features a correct design flow angle only at the outlet section. Therefore, to attain the nominal flow angle along the centerline of the diverging section, a conformal mapping [30] is applied (see black nozzle with side n_a and n_b in Fig. 3). The conformally mapped co-ordinates (x', y') can be written as

$$x' = Ae^{Bt}\cos(t), \quad y' = Ae^{Bt}\sin(t), \tag{8}$$

where A is the radius of the last point of the axial centerline lying on the logarithmic spiral, B is $\tan^{-1}(\phi)$, and t ranges from $0 - N\pi$.

(3) *Rotate the suction side of the diverging section by the pitch angle*. In order to have the suction and the pressure side belonging to the same stator vane, the diverging section curve n_b is rotated by the pitch angle, as can be seen in Fig. 3.

(4) *Construct the converging section*. The converging section of the nozzle is designed with three circular arcs centered at C1, C2, and C3 (see Fig. 4). The center C1 and C2 lie on

the perpendicular lines on the two sides of the curved center line. The radius of the circle centered in C1 is taken such as to be tangent to the outer circumference of radius R_{in}. Similarly, the circle with center C2 is defined with the same radius as the one with center C1. The arcs with center C1 and C2 are extended such to guarantee C^1 continuity with the arc centered in C3. Typical values for the angles subtended by the two arcs centered in C1 and C2 are 3.5 and 0.2 rad, respectively. This procedure is only one of the several that can be adopted to create the shape of the vane converging section. However, with respect to procedures involving the use of nonuniform rational basis spline curves, the method here described has the advantage of ease of implementation.

(5) *Construct the semibladed section of the suction side*. The diverging suction side of the nozzle is constructed through a line departing from n_{a2} and preserving the flow angle ϕ up to R_{out}. The resulting trailing-edge thickness, i.e., the Euclidean distance between points n_{a3}, n_{b2}, is therefore a function of the scaling factor S. In particular, there exists a S value yielding the user-specified thickness dx.

The above problem is solved by means of a minimization with S as design variable. The cost function to minimize reads

$$\min_S \quad J = d(n_{a3}(S), n_{b2}(S)) - dx \tag{9}$$

in which J is the difference between the distance n_{a3}, n_{b2} and dx, where dx is the minimum allowable trailing-edge thickness usually selected according to manufacturing constraints (cf. Fig. 4). Table 1 summarizes the input parameters of the procedure.
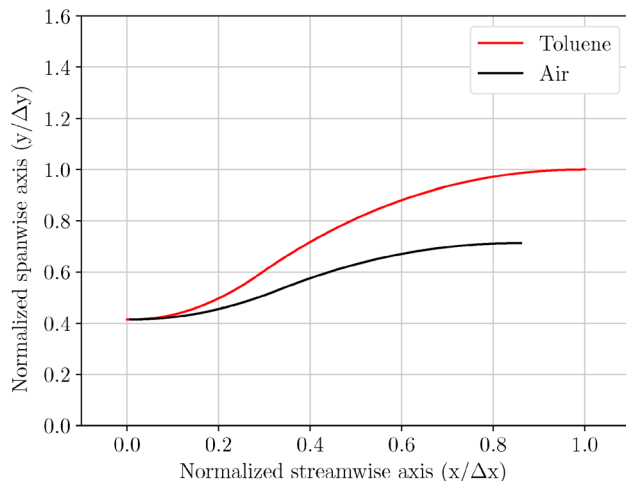
Fig. 2 Comparison of nozzle shape for air and Toluene (using MoC)
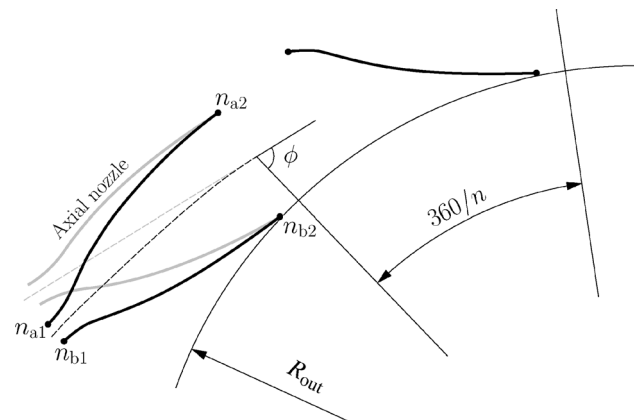
Fig. 3 Steps illustrating the design of supersonic radial stator. The axial nozzle from MoC is transformed to the radial inlet design and rotated by the pitch angle (i.e., 360/n).
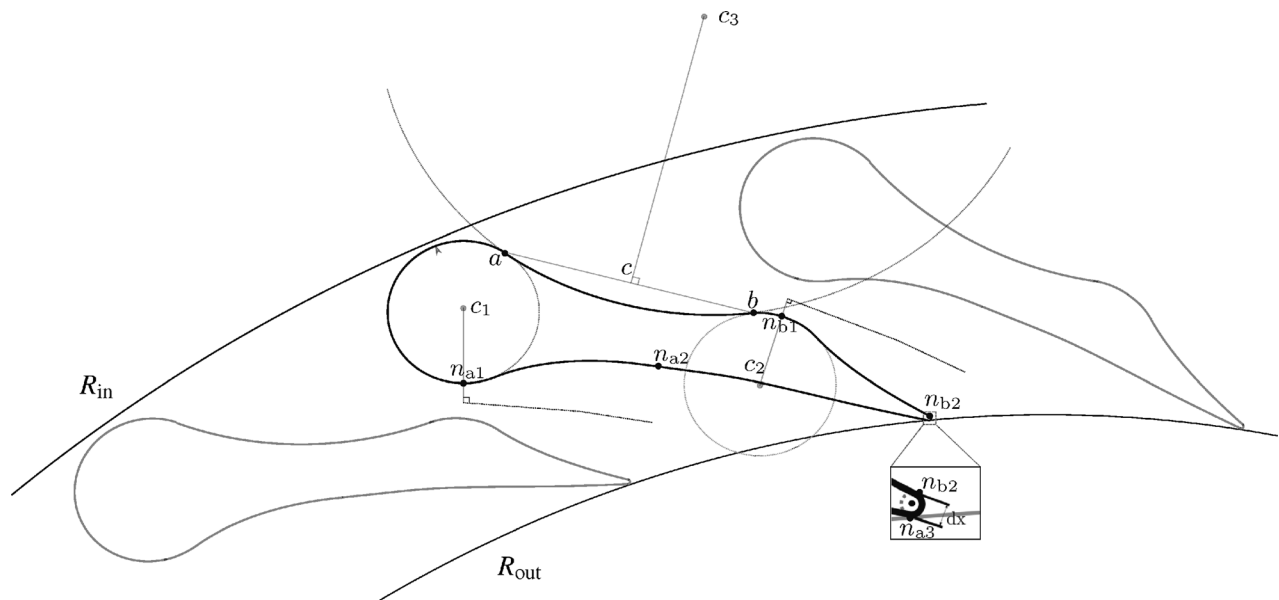
Fig. 4 Geometrical construction of the supersonic radial stator vane. The gray vanes are the copy of the black vane rotated by the pitch angle on the either sides.

Figure 4 shows an example of supersonic stator vane row accomplished by means of the described method.

3 Case Study

The method described above has been applied to design a supersonic radial vane of the turbine of a commercial ORC unit delivering $200\,kW_e$ at nominal conditions. The expansion ratio of the vane is 40 and the working medium is Toluene. The compressibility factor close to the nozzle throat is 0.75 and the Reynolds number of the flow is 10^6 based on throat width. The boundary conditions, i.e., P_{tot}, T_{tot}, Ma, and the specifications (e.g., ϕ) needed for the vane design are not reported here for confidentiality reasons.

It is worth noting that the reported Reynolds number is deemed sufficiently high to neglect boundary layer blockage effects in the design of the nozzle. For the considered turbine application, the boundary layer blockage factor, defined as ratio of boundary layer displacement thickness over the flow passage width, is estimated to be about 2% at the nozzle exit section.

In order to demonstrate the effectiveness of the proposed methodology, the fluid dynamic performance of the newly designed stator is compared to that of two vane configurations previously realized and tested for the same turbine. The first geometry, which is illustrated in Ref. [31], was obtained by using empirical rules and engineering practices. The second was a redesign of the original one by applying CFD-based shape optimization [23]. The mass-averaged Mach number Ma at the outlet section of the bladed nozzle resulted from Ref. [23] is assigned as input for the method described in this work. The design is done for the operating point, without taking into account off-design performance or manufacturing uncertainties. For the sake of clarity, the first

Table 1 Input parameter for stator design methodology

	Parameter	Description	Units
1	Flow angle	Stator exit metal angle	(deg)
2	No. of vanes	Number of stator vanes	
3	Inlet radius	UL stator radius	(m)
4	Outlet radius	LL stator radius	(m)
5	Thickness	Trailing edge thickness	(m)

Note: UL: upper limit, LL: lower limit.

design will be referred to as *baseline*, the second to as *shape—optimized*, and the one obtained with the new method as *MoC—based*. The three stator geometries are illustrated in Fig. 5.

3.1 Numerical Model. The performance of the three geometries is computed using a CFD model based on Reynolds Averaged Navier–Stokes equations [32–34]. The computational domain, highlighted in gray in Fig. 6, is discretized by using an unstructured grid composed of hexahedral elements. The cell elements were clustered so as to ensure a y^+ below unity. The thermophysical properties of the working fluid are computed with the Span–Wagner model available in FluidProp [29] using a look-up table approach [35]. The turbulent quantities are modeled with the Spalart–Allmaras [36] turbulence model, which has been adopted for simulating ORC machines in past [18].

3.2 Mesh Convergence Study. To ensure mesh independent results, a grid convergence study was performed using the Richardson extrapolation method as proposed in Ref. [37].
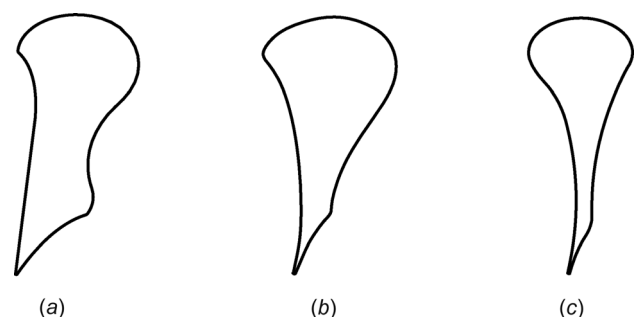
The essential parameter required for conducting a mesh convergence study is the mesh size represented by h_i where $i = 1$, 2, 3 denotes the fine, medium, and coarse grids, respectively. The ratios of the mesh size are termed grid refinement factors r.

The discretization error ε was calculated by computing the difference between the numerical simulations (in this case total pressure loss coefficients) f for the grids i, $i + 1$, i.e., $\varepsilon_{i+1,i} = f_{i+1} - f_i$. As in this study a monotonic convergence can be observed, the


Fig. 5 Stator vane geometries: (a) baseline, (b) shape-optimized, and (c) MoC-based
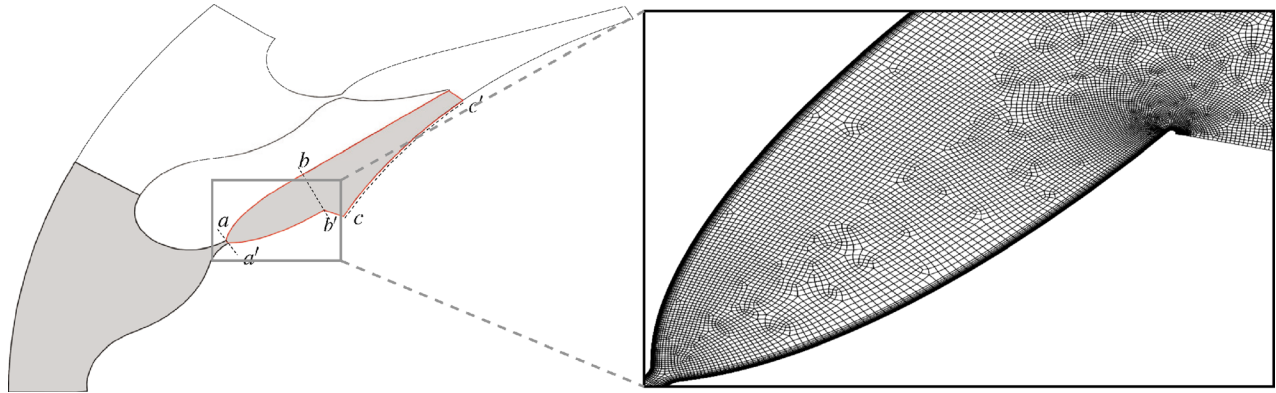
Fig. 6 Geometry [left] and mesh [right] of the baseline stator. The shaded area in the geometry represents one flow passage in the stator. The flow passage downstream of the throat is representative of the area for which the solution has been reported in this work. *aa′*; *bb′*, and *cc′* are the cross sections across which the pressure ratios are reported.
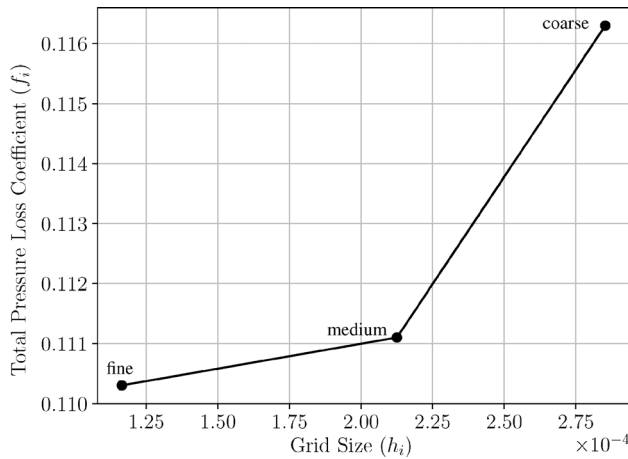
Fig. 7 Variation of solution with grid size

following relation is used for calculating the apparent order of convergence (p) of the method

$$p = \frac{1}{\ln(r)} \cdot \left| \ln \left| \frac{\varepsilon_{32}}{\varepsilon_{21}} \right| + \ln \frac{r_{21}^p - 1}{r_{32}^p - 1} \right| \qquad (10)$$

Equation (10) is an implicit equation and is solved iteratively. Using the apparent order of the solution p, the refinement ratios r and f, the extrapolated value (f_{ext}) of the properties can be calculated using:

$$f_{\text{ext}}^{21} = (r_{21}^p f_1 - f_2)/(r_{21}^p - 1) \qquad (11)$$

Finally, the approximate (e_a), extrapolated relative errors (e_{ext}) and grid convergence index (GCI) [38] were calculated using the below equation:

$$e_a^{21} = |f_1 - f_2|, \quad e_{\text{ext}}^{21} = \left| \frac{f_{\text{ext}}^{21} - f_1}{f_{\text{ext}}^{21}} \right|, \quad \text{GCI}_{\text{fine}}^{21} = \frac{F_s \cdot e_a^{21}}{r_{21}^p - 1} \qquad (12)$$

A factor of safety value of (F_s) 3.0 is used as recommended in Ref. [39]. The three meshes employed to estimate the

Table 3 Expansion ratio at different sections of the stator

Stators	β_{blade}	β_{post}
Baseline	5.13	0.79
Shape optimized	2.36	1.68
MoC-based	2.41	1.67

discretization error are constituted by 37,873, 68,242, and 227,322 elements, respectively. The variation of f_i with grid size (h_i) is illustrated in Fig. 7.

From the results shown in Table 2, it can be concluded that mesh 2 has an uncertainty of 1.93% and can be deemed sufficient for the purpose of this work.

3.3 Results. The numerical results for the three stator geometries are documented in this section. The solutions are compared qualitatively in terms of flow features and quantitatively by the performance parameters expressed in terms of total pressure (Y), entropy production (s_{gen}), and kinetic energy loss (ζ) coefficient. The three coefficients are calculated using mass averaged inlet and exit properties for enthalpy ($\bar{h}$), entropy ($\bar{s}$), velocity ($\bar{v}$), and pressure ($\bar{p}$), defined as:

$$Y = \frac{\bar{p}_{\text{tot,in}} - \bar{p}_{\text{tot,out}}}{\bar{p}_{\text{tot,in}} - \bar{p}_{\text{out}}} \qquad (13a)$$

$$s_{\text{gen}} = \frac{\bar{s}_{\text{out}} - \bar{s}_{\text{in}}}{\bar{s}_{\text{in}}} \qquad (13b)$$

$$\zeta = \frac{\bar{h}_{\text{out}} - \bar{h}_{\text{is,out}}}{\left(\bar{v}_{\text{is,out}} \right)^2} \qquad (13c)$$

where superscript "is" represents isentropic conditions and, "in" and "out" represent properties at the inlet and outlet boundaries.

As well established in literature, see for instance Ref. [40], the key design parameter affecting the fluid-dynamic performance of a supersonic vane is the degree of postexpansion (β_{post}), which in turn is a function of the throat to nozzle outlet section ratio. By varying β_{post}, the losses due to viscous friction within the diverging section boundary layers and to the fishtail shock-wave

Table 2 Mesh independence study for the present work

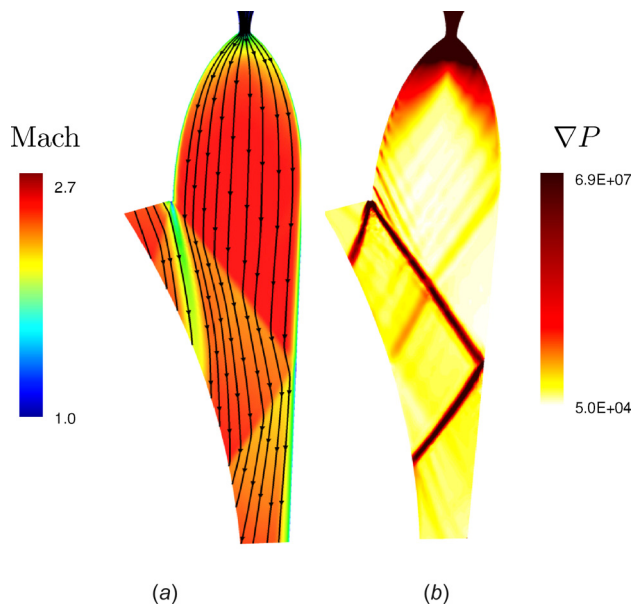| Parameters	r_{21}	r_{32}	f_1	f_2	f_3	p	f_{ext}^{21}	e_a^{21}	e_{ext}^{21}	$\text{GCI}_{\text{fine}}^{21}$
Values	1.34	1.82	0.1103	0.1111	0.1163	2.50	0.1096	0.70%	0.65%	1.93%

Fig. 8 CFD results of the baseline stator: (a) Mach number contour and (b) pressure gradient contour

Table 4 Performance coefficients for the three stator

Stator	Y	s_{gen}	ζ
Baseline	0.19	0.012	0.028
Shape optimized	0.12	0.009	0.020
MoC-based	0.11	0.008	0.016

stemming from either side of the trailing edge can be minimized. The value of β_{post} is reported in Table 3 along with the expansion ratio in the bladed region (β_{blade}). The ratios are calculated as $\beta_{blade} = P_{bb'}/P_{aa'}$, $\beta_{post} = P_{cc'}/P_{bb'}$; where aa', bb', and cc' are the cross sections illustrated in Fig. 6.

It can be observed that in the MoC-based and shape-optimized stator the flow expands both in the bladed and in the semibladed
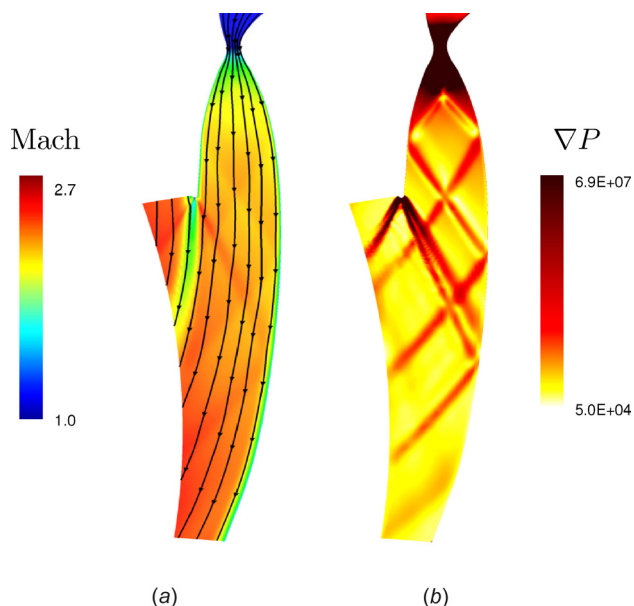

Fig. 9 CFD results of the Shape-optimized stator: (a) Mach number contour and (b) pressure gradient contour
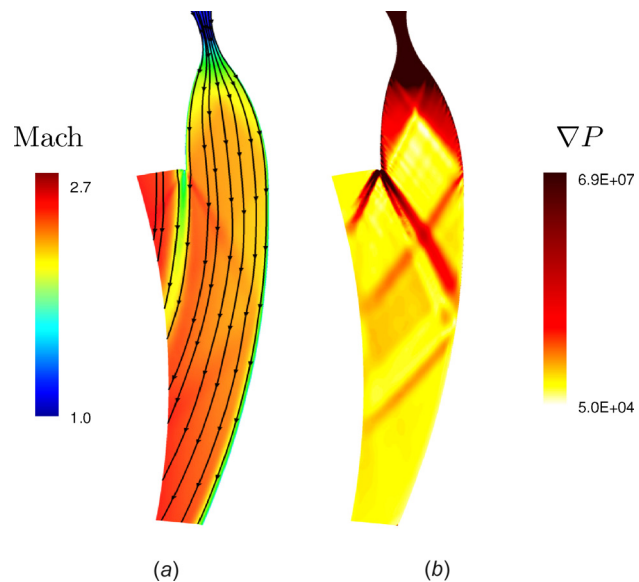
Fig. 10 CFD results of the MoC-Based stator: (a) Mach number contour and (b) pressure gradient contour

region. As expected, β_{post} is similar in these two configurations, meaning that the fluid-dynamic performance of the two vanes is arguably equivalent. In contrast, the baseline stator features a postcompression in the semibladed section, which leads to the formation of stronger shock waves at the trailing edge, see Fig. 8(a). This is caused by the excessively large expansion ratio in the diverging channel, which is eventually related to the nozzle throat-to-exit area ratio. This parameter must then be selected carefully to prevent the onset of highly dissipative phenomena in supersonic vanes.

The previous considerations have been confirmed by the computed performance coefficients, reported in Table 4. It can be inferred that the large improvement in fluid-dynamic performance, as compared to the original vane geometry, can be primarily attributed to the weakening of shock-wave strength, which ultimately reduces the entropy generation over the mixing process downstream of the blade, see Figs. 9(a) and 10(a). Conversely, the MoC-based and the shape-optimized are characterized by similar performance. This is furthermore pointed out by the nondimensional averaged exit Mach number and flow angle, reported in Table 5. Yet, the results obtained for baseline stator are worse than the other designs. Quasi three-dimensional steady CFD simulations were used to quantitatively assess the impact of the MoC-based stator on the overall turbine efficiency. The results showed 1.5% total-to-total efficiency increment as compared to baseline design.

The advantages of the MoC-based as compared to the shape-optimized method become more evident by looking at the Mach number and flow angle pitch-wise distribution at the nozzle outlet boundary, see Figs. 11(a) and 11(b). In particular, the shape-optimized configuration features a larger Mach number nonuniformity for $\Delta\theta/\theta < 0.4$ and or $\Delta\theta/\theta > 0.7$. It can be observed that in these two regions, the flow exhibits repeated pressure fluctuations caused by the existence of four pressure waves on the outlet

Table 5 Average exit properties for the three stator

Stator	ϕ/ϕ_{design}	M/Ma
Baseline	1.05	0.99
Shape-optimized	1.01	1.00
MOC-based	1.02	1.00
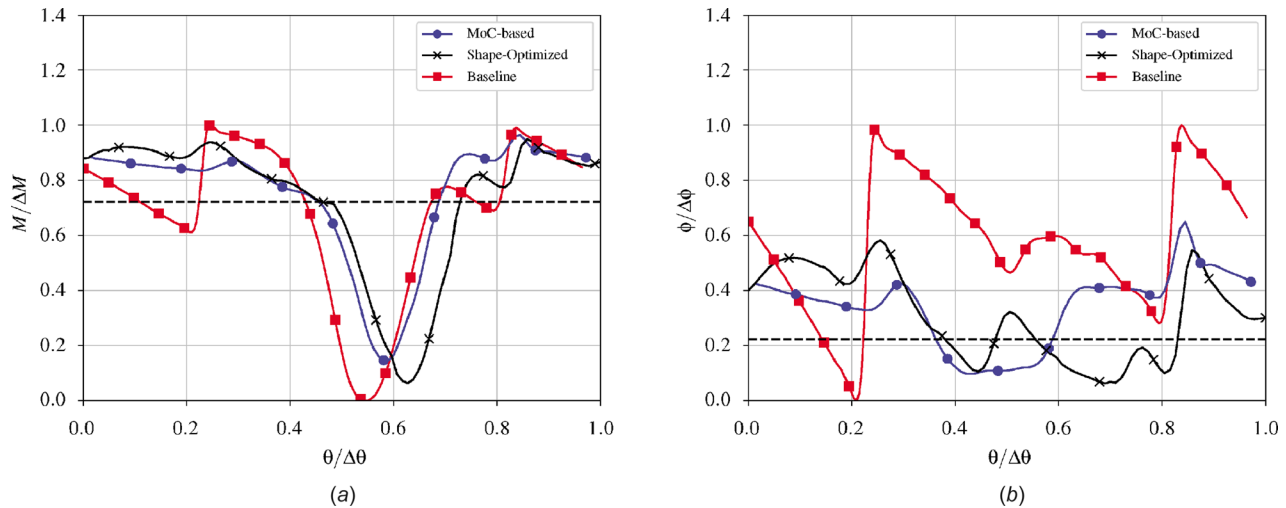
Fig. 11 Instantaneous stator exit property distribution. $\theta/\Delta\theta = 0$ and 1 represent stator outlets at two adjacent vane trailing edges. Dashed lines represent target values: (a) Mach number and (b) flow angle.
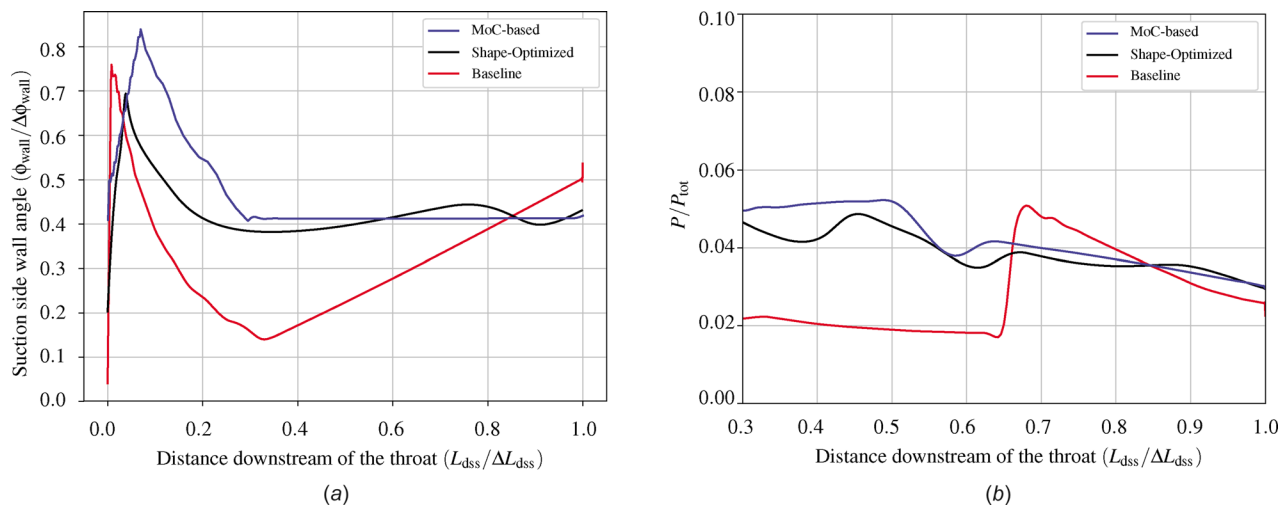
Fig. 12 Instantaneous property variation on the suction side wall, downstream of the throat. $L_{dss}/\Delta L_{dss} = 0$ represents the throat and $L_{dss}/\Delta L_{dss} = 1$ represents stator trailing edge, where ΔL_{dss} = distance between points n_{a1} and n_{a3} in Fig. 4: (a) wall angle and (b) static pressure.

boundary. The former and the latter are the usual trailing-edge shock-wave, but the remaining two originate from the conjunction of compression waves induced by the excessive concavity of the final part of the diverging bladed section. In the case of the MoC-based geometry, only three waves appear, with the middle one comparatively much weaker. Despite the similar mean flow angle downstream of the blade for the shape-optimized and for the MoC-based geometry, the local flow angle distribution at the outlet boundary (see Fig. 11(b)) is significantly altered by the presence of four waves. This is likely to have detrimental effects on the fluid-dynamic performance of the subsequent rotor, which is bound to operate under highly nonuniform inlet flow conditions.

Further insights can be gained by examining the wall angle distribution (flow angle made by the streamline close to the wall with the center of rotation) of the semibladed region. As shown in Fig. 12(a), the averaged wall angle for shape-optimized geometry resembles the constant wall angle imposed in the MoC-based method, suggesting that, as recommended in Ref. [41] for supersonic ORC axial cascades, the profile of the rear suction side needs to be designed with a constant wall angle also for radial

vanes. Note that the Mach number reported in Fig. 11(a) jumps at $\theta/\Delta\theta = 0.8$ caused by the reflected trailing-edge shock wave is more pronounced in the shape-optimized configuration. This can be attributed to the shape of the semibladed profile between $L_{dss}/\Delta L_{dss} = 0.4$ and 0.6, see Fig. 12(a), whose local wall angle distribution entails a flow over acceleration, which eventually leads to a stronger oblique shock wave at $L_{dss}/\Delta L_{dss} = 0.65$ in reported Fig. 12(b). The design aspect that may need improvement in the MoC-based geometry is the transition between the bladed and the semibladed section, which is now characterized by a marked geometrical first-order discontinuity. Nonetheless, according to the results, its impact on the fluid-dynamic performance of the vane can be deemed negligible.

Remarkably, all these results point out that in supersonic radial vanes, the global fluid-dynamic performance of the cascade is not the only figure of merit, and in order to reduce the local flow non-uniformity, great attention must be paid to every geometrical detail of the bladed and nonbladed region. As proven, regardless, the use of a method combining shape optimization and a physical model suitable for nonideal compressible flows can provide the

optimal postexpansion ratio for a given supersonic vane application, it is not guaranteed that the shape of the optimized channel yields the best fluid-dynamic performance.

4 Conclusion

A novel design methodology, referred to as MoC-based, for supersonic radial vanes operating with nonideal compressible flows is illustrated in this work. The geometry of the supersonic vane is accomplished by conformally mapping the diverging section obtained via the method of characteristics adapted for nonideal compressible flows and constructing the converging part through a dedicated geometrical procedure.

The capability of the methodology has been investigated by designing the supersonic vane of a high-loaded organic Rankine cycle turbine, for which two vane geometries already existed. The former was designed using empirical rules and engineering practices, while the second one resulted from a shape optimization procedure based on an inviscid flow model.

The results of the study have pointed out that, for the case study considered, the fluid-dynamic performance of the MoC-based vane geometry outperforms both the original and the shape-optimized one. Improvement in MoC-based stator corresponds to 1.5% total-to-total turbine efficiency compared to baseline design. It can be then inferred that the proposed MoC-based design procedure for nonideal flows is suitable for the design of supersonic vanes at comparatively lower cost than that required by CFD-based optimization techniques. This is particularly advantageous when applications involving nonideal flows are of concern, as the usual cost of a single CFD run with accurate thermodynamic models is significantly larger than that for a perfect gas model.

In summary, two major points can be outlined from the study (i) the degree of postexpansion is the key parameter affecting the fluid-dynamic efficiency of a supersonic radial vane and it is therefore advisable to select it through parametric studies (ii) for vanes experiencing similar degree of postexpansion, the correct detailed design of the diverging as well as the semibladed region is essential to reduce flow nonuniformity, which is highly detrimental for the performance of the subsequent blade row. Despite the complexity of the flow pattern in supersonic radial vanes, the proposed method is capable of providing quasi-uniform flow downstream of the nozzle.

Acknowledgment

Nomenclature

Symbols

a, b = constants
A = primary radius of the logarithmic spiral
B = angle preserved by the logarithmic spiral
c = speed of sound
dx = trailing edge thickness
e = relative error
f = numerical solution
h = mesh size
H = enthalpy
$\bar{h}$ = mass average enthalpy
J = distance between trailing edges
L = distance
Ma = design Mach number
n = number of stator vanes
N = number of rotations
p = apparent power
P = pressure
$\bar{p}$ = mass average pressure
r = refinement factor
s = entropy
S = scaling factor
$\bar{s}$ = mass average entropy
t = azimuthal angle of logarithmic spiral
T = temperature
u, v = velocity components
V = velocity magnitude
x, y = position co-ordinates
x', y' = conformed position co-ordinates
Y = pressure loss coefficient

Greek Symbols

α = Mach angle
β = pressure ratio
Δ = difference
ε = error in the meshes
ζ = kinetic energy loss coefficient
θ = azimuthal angle
λ = characteristics slope
∇ = gradient
ρ = density
ϕ = flow angle

Subscripts

a = approximate
blade = bladed
design = design
dss = downstream, suction-side
ext = extrapolated
gen = generation
i = grid number
in = inlet
is = isentropic
out = outlet
post = post
tot = total conditions
wall = wall

Superscript

$1..3$ = reference grid number

References

[1] Whitfield, A., and Baines, N. C., 1990, *Design of Radial Turbo-Machines*, Longman Scientific & Technical, New York.
[2] Karamanis, N., and Martinez-Botas, R. F., 2002, "Mixed-Flow Turbines for Automotive Turbochargers: Steady and Unsteady Performance," Int. J. Engine Res, **3**(3), pp. 127–138.
[3] Chebli, E., Casey, M., Martinez-Botas, R., Sumser, S., Müller, M., Künzel, S., Leweux, J., Gorbach, A., and Schmidt, W., 2014, "The Variable Outlet Turbine Concept for Turbochargers," ASME J. Turbomach., **136**(12), p. 121001.
[4] Fu, L., Feng, Z., and Li, G., 2017, "Experimental Investigation on Overall Performance of a Millimeter-Scale Radial Turbine for Micro Gas Turbine," Energy, **134**, pp. 1–9.
[5] Mack, Y., Haftka, R., Griffin, L., Snellgrove, L., Dorney, D., Huber, F., and Shyy, W., 2006, "Radial Turbine Preliminary Aerodynamic Design Optimization for Expander Cycle Liquid Rocket Engine," AIAA Paper No. 2006-5046.
[6] Bufi, E. A., Obert, B., and Cinnella, P., 2015, "Fast Design Methodology for Supersonic Rotor Blades With Dense Gas Effects," Third International Seminar on ORC Power Systems, Brussels, Belgium, Oct. 12–14, Paper No. 34.
[7] Paniagua, G., Iorio, M., Vinha, N., and Sousa, J., 2014, "Design and Analysis of Pioneering High Supersonic Axial Turbine," Int. J. Mech. Sci., **89**, pp. 65–77.
[8] Goldman, L. J., and Scullin, V. J., 1968, "Analytical Investigation of Supersonic Turbo-Machinery Blading—I: Computer Program for Blading Design," NASA Lewis Research Center, Cleveland, OH, Report No. NASA-TN D-4421.
[9] Goldman, L. J., 1968, "Analytical Investigation of Supersonic Turbo-Machinery Blading—II: Analysis of Impulse Turbine-Blade Sections," NASA Lewis Research Center, Cleveland, OH, Report No. NASA TN D-4422.
[10] Sauret, E., and Rowlands, A., 2011, "Candidate Radial-Inflow Turbines and High-Density Working Fluids for Geothermal Power Systems," Energy, **36**(7), pp. 4460–4467.

[11] Verma, R., Sam, A. A., and Ghosh, P., 2015, "CFD Analysis of Turbo Expander for Cryogenic Refrigeration and Liquefaction Cycles," Phys. Procedia, **67**, pp. 373–378.

[12] Colonna, P., Casati, E., Trapp, C., Mathijssen, T., Larjola, J., Turunen-Saaresti, T., and Uusitalo, A., 2015, "Organic Rankine Cycle Power Systems: From the Concept to Current Technology, Applications, and an Outlook to the Future," ASME J. Eng. Gas Turbines Power, **137**(10), p. 100801.

[13] Harinck, J., Pasquale, D., Pecnik, R., Van Buijtenen, J., and Colonna, P., 2013, "Performance Improvement of a Radial Organic Rankine Cycle Turbine by Means of Automated Computational Fluid Dynamic Design," Proc. IMechE Part A: J. Power Energy, **227**(6), pp. 637–645.

[14] White, M., and Sayma, A., 2016, "Improving the Economy-of-Scale of Small Organic Rankine Cycle Systems Through Appropriate Working Fluid Selection," Appl. Energy, **183**, pp. 1227–1239.

[15] Bahamonde, S., Pini, M., De Servi, C., Rubino, A., and Colonna, P., 2017, "Method for the Preliminary Fluid Dynamic Design of High-Temperature Mini-Organic Rankine Cycle Turbines," ASME J. Eng. Gas Turbines Power, **139**(8), p. 082606.

[16] Colonna, P., Harinck, J., Rebay, S., and Guardone, A., 2008, "Real-Gas Effects in Organic Rankine Cycle Turbine Nozzles," J. Propul. Power, **24**(2), pp. 282–294.

[17] Gori, G., Vimercati, D., and Guardone, A., 2017, "Non-Ideal Compressible-Fluid Effects in Oblique Shock Waves," J. Phys. Conf. Ser., **821**(1), p. 012003.

[18] Rinaldi, E., Pecnik, R., and Colonna, P., 2016, "Unsteady Operation of a Highly Supersonic Organic Rankine Cycle Turbine," ASME J. Turbomach., **138**(12), p. 121010.

[19] Wheeler, A. P. S., and Ong, J., 2013, "The Role of Dense Gas Dynamics on ORC Turbine Performance," ASME J. Eng. Gas Turbines Power, **135**(10), p. 082604.

[20] Kang, S. H., "Design and Experimental Study of ORC (Organic Rankine Cycle) and Radial Turbine Using R245fa Working Fluid," J. Energy, **41**(1), pp. 514–524.

[21] Pini, M., Servi, C. D., Burigana, M., Rubino, A., Vitale, S., and Colonna, P., "Fluid-Dynamic Design and Characterization of a Mini-ORC Turbine for Laboratory Experiments," Energy Procedia, **129**, pp. 1141–1148.

[22] Uusitalo, A., Turunen-Saaresti, T., Guardone, A., and Grönman, A., 2014, "Design and Flow Analysis of a Supersonic Small Scale ORC Turbine Stator With High Molecular Complexity Working Fluid," ASME Paper No. GT2014-26204.

[23] Pasquale, D., Ghidoni, A., and Rebay, S., 2013, "Shape Optimization of an Organic Rankine Cycle Radial Turbine Nozzle," ASME J. Eng. Gas Turbines Power, **135**(4), p. 042308.

[24] Guardone, A., Spinelli, A., and Dossena, V., 2013, "Influence of Molecular Complexity on Nozzle Design for an Organic Vapor Wind Tunnel," ASME J. Eng. Gas Turbines Power, **135**(4), p. 042307.

[25] Zucrow, M. J., and Hoffman, J. D., 1976, *Gas Dynamics*, Vol. 1, Wiley, Hoboken, NJ.

[26] Zucrow, M. J., and Hoffman, J. D., 1977, *Gas Dynamics Volume 2: Multidimensional Flow*, Vol. 2, Wiley, Hoboken, NJ.

[27] Sauer, R., 1947, "General Characteristics of the Flow Through Nozzles at Near Critical Speeds," National Advisory Committee for Aeronautics, Washington DC, Report No. NACA-TM-1147.

[28] Span, R., and Wagner, W., 2003, "Equations of State for Technical Applications—II: Results for Non-Polar Fluids," Int. J. Thermophys., **24**(1), pp. 41–109.

[29] Colonna, P., and van der Stelt, T. P., 2004, "FluidProp: A Program for the Estimation of Thermo Physical Properties of Fluids," *Energy Technology Section*, Delft University of Technology, Delft, The Netherlands.

[30] Archibald, R. C., 1918, "The Logarithmic Spiral," Am. Math. Mon., **25**(8), pp. 189–193.

[31] Harinck, J., Pecnik, R., and Colonna, P., 2012, "Three-Dimensional RANS Simulation of an Organic Rankine Cycle Turbine," Delft University of Technology, Delft, The Netherlands, P&E Report No. 2572.

[32] Rinaldi, E., Pecnik, R., and Colonna, P., 2014, "Exact Jacobians for Implicit Navier–Stokes Simulations of Equilibrium Real Gas Flows," J. Comput. Phys., **270**, pp. 459–477.

[33] Pecnik, R., Terrapon, V. E., Ham, F., Iaccarino, G., and Pitsch, H., 2012, "Reynolds-Averaged Navier-Stokes Simulations of the HyShot II Scramjet," AIAA J., **5**(8), pp. 1717–1732.

[34] Pecnik, R., Rinaldi, E., and Colonna, P., 2012, "Computational Fluid Dynamics of a Radial Compressor Operating With Supercritical CO_2," ASME J. Eng. Gas Turbines Power, **134**(12), p. 122301.

[35] Rinaldi, E., Pecnik, R., and Colonna, P., 2012, "Accurate and Efficient Look-Up Table Approach for Dense Gas Flow Simulations," Sixth European Congress on Computational Methods in Applied Sciences and Engineering (ECCOMAS 2012), Vienna, Austria, Sept. 10–14, pp. 8690–8704.

[36] Spalart, P. R., and Allmaras, S. R., 1992, "A One-Equation Turbulence Model for Aerodynamic Flows," AIAA Paper No. 1992-439.

[37] ASME, 2009, "Standard for Verification and Validation in Computational Fluid Dynamics and Heat Transfer," American Society of Mechanical Engineers, New York.

[38] Roache, P., 1997, "Quantification of Uncertainty in Computational Fluid Dynamics," Annu. Rev. Fluid Mech., **29**(1), pp. 123–160.

[39] Franke, J., and Frank, W., 2008, "Application of Generalized Richardson Extrapolation to the Computation of the Flow Across an Asymmetric Street Intersection," J. Wind Eng. Ind. Aerodyn., **96**(10–11), pp. 1616–1628.

[40] Deich, M. E., Filippov, G. A., and Lazarev, L. Y., 1965, *Atlas of Axial Turbine Blade Characteristics*, Mashinostroenie Publishing House, Moscow, Russia.

[41] Pini, M., Persico, G., Pasquale, D., and Rebay, S., 2014, "Adjoint Method for Shape Optimization in Real-Gas Flow Applications," ASME. J. Eng. Gas Turbines Power, **137**(3), p. 032604.